



## Article

# A Flexible Lithium-Ion-Conducting Membrane with Highly Loaded Titanium Oxide Nanoparticles to Promote Charge Transfer for Lithium–Air Battery

Si-Han Peng <sup>1</sup>, Yen-Hsiang Yu <sup>1</sup>, Hsin-Chun Lu <sup>1,\*</sup>  and Shingjiang Jessie Lue <sup>1,2,3,\*</sup> 

<sup>1</sup> Department of Chemical and Materials Engineering, Chang Gung University, Guishan District, Taoyuan City 333, Taiwan; d1123003@cgu.edu.tw (S.-H.P.); sean0229530699@gmail.com (Y.-H.Y.)

<sup>2</sup> Department of Orthopedics, Chang Gung Memorial Hospital, Linkou, Guishan District, Taoyuan City 333, Taiwan

<sup>3</sup> Department of Safety, Health and Environmental Engineering, Ming-Chi University of Technology, Taishan District, New Taipei City 243, Taiwan

\* Correspondence: hsinchun@mail.cgu.edu.tw (H.-C.L.); jessie@mail.cgu.edu.tw (S.J.L.)

**Abstract:** In this research, we aim to investigate a flexible composite lithium-ion-conducting membrane (FC-LICM) consisting of poly(vinylidene fluoride-co-hexafluoropropylene) (PVDF-HFP) and titanium dioxide (TiO<sub>2</sub>) nanoparticles with a TiO<sub>2</sub>-rich configuration. PVDF-HFP was selected as the host polymer owing to its chemically compatible nature with lithium metal. TiO<sub>2</sub> (40–60 wt%) was incorporated into the polymer matrix, and the FC-LICM charge transfer resistance values (R<sub>ct</sub>) were reduced by two-thirds (from 1609 Ω to 420 Ω) at the 50 wt% TiO<sub>2</sub> loading compared with the pristine PVDF-HFP. This improvement may be attributed to the electron transport properties enabled by the incorporation of semiconductive TiO<sub>2</sub>. After being immersed in an electrolyte, the FC-LICM also exhibited a R<sub>ct</sub> that was lower by 45% (from 141 to 76 Ω), suggesting enhanced ionic transfer upon the addition of TiO<sub>2</sub>. The TiO<sub>2</sub> nanoparticles in the FC-LICM facilitated charge transfers for both electron transfer and ionic transport. The FC-LICM incorporated at an optimal load of 50 wt% TiO<sub>2</sub> was assembled into a hybrid electrolyte Li–air battery (HELAB). This battery was operated for 70 h with a cut-off capacity of 500 mAh g<sup>−1</sup> in a passive air-breathing mode under an atmosphere with high humidity. A 33% reduction in the overpotential of the HELAB was observed in comparison with using the bare polymer. The present work provides a simple FC-LICM approach for use in HELABs.

**Keywords:** flexible lithium-ion-conducting membrane; solid polymer composite; hybrid electrolyte lithium–air battery; charge transfer; titanium dioxide nanoparticles



check for updates

**Citation:** Peng, S.-H.; Yu, Y.-H.; Lu, H.-C.; Lue, S.J. A Flexible Lithium-Ion-Conducting Membrane with Highly Loaded Titanium Oxide Nanoparticles to Promote Charge Transfer for Lithium–Air Battery. *Polymers* **2023**, *15*, 2409. <https://doi.org/10.3390/polym15102409>

Academic Editor: Claudio Gerbaldi

Received: 17 March 2023

Revised: 13 May 2023

Accepted: 18 May 2023

Published: 22 May 2023



**Copyright:** © 2023 by the authors. Licensee MDPI, Basel, Switzerland. This article is an open access article distributed under the terms and conditions of the Creative Commons Attribution (CC BY) license (<https://creativecommons.org/licenses/by/4.0/>).

## 1. Introduction

With the increasing demand for electronic devices, electric vehicles, and large-scale electrochemical storage systems, lithium-ion batteries cannot fully satisfy industrial needs, which is primarily due to their insufficient energy density [1]. Non-aqueous Li–air batteries have attracted research efforts because of their superior theoretical energy density [2]. Despite this, such batteries suffer from the flammability of the volatile organic liquid electrolyte (LE), along with the latent decomposition found in conventional lithium-ion batteries [3]. One serious problem is that the solid reaction product (Li<sub>2</sub>O or Li<sub>2</sub>O<sub>2</sub>) is insoluble in aprotic electrolytes, which hinders its practical development [4–8]. A Li–air battery with a hybrid electrolyte was therefore designed to avoid these detrimental effects [9–12].

Hybrid electrolyte Li–air batteries (HELABs) consist of an organic LE at the lithium anode side, a solid-state electrolyte (a lithium-ion conductive membrane (LICM)) in the middle to prevent intermixing, and an aqueous LE at the cathode side. HELABs have a Li/organic electrolyte/sodium super ionic conductor glass film (NASICON)/aqueous

electrolyte/cathode structure. The HELAB directly addresses the aforementioned problems by mitigating the flammability and volatilization of aprotic LE, with the discharge product (LiOH) being soluble in an aqueous LE. In addition, HELABs can be operated under an ambient atmosphere with high relative humidity, thereby saving the cost of the high-purity O<sub>2</sub> supply device required in aprotic Li–air batteries [13,14]. The most common oxides used for an LICM are NASICON-type materials such as Li<sub>1+x</sub>Al<sub>x</sub>Ti<sub>2-x</sub>(PO<sub>4</sub>)<sub>3</sub> (LATP) and Li<sub>1+x</sub>Al<sub>x</sub>Ge<sub>2-x</sub>(PO<sub>4</sub>)<sub>3</sub> (LAGP). However, due to its rigid nature, a ceramic LICM has a risk of cracking during assembly, followed by electrolyte leakage, corrosion of the lithium, and deterioration of the battery [13,14].

Recently, researchers have prepared solid polymer electrolytes (SPE) to take advantage of the synergistic properties of polymer–nanoparticle hybrid compositions [15]. The polymer matrix improves the mechanical properties, while the nanoparticles provide continuous pathways, enabling high ionic conductivity [16–18]. In order to achieve a large specific surface area and a drastic increase in the conductivity of the hybrid composites, nanoscale fillers are prepared via many methods, such as hydrothermal [19], in-situ sol-gel [20], and electrospinning methods [16,18]. Among them, ball-milling is a simple process for reducing the grain size of clustering nanoparticles and increasing the particles' dispersivity [21]. The polymer electrolyte can be fabricated by dispersing the ceramic into a polymer matrix. The concentration of ceramic filler is small and typically has a low weight percentage relative to the polymer host [22,23]. An interesting concept called the “polymer-in-ceramic” configuration is attracting much attention by integrating a high concentration of ceramic nanoparticles into the polymer matrixes. For instance, Chen et al. studied poly(ethylene oxide) (PEO)-based SPE with the addition of ceramic at a concentration of 10 wt% to 80 wt%. The ionic conductivity gradually decreased with the increase in the proportion of the weight of the ceramic [24]. However, Zhang et al. prepared a flexible and free-standing SPE by integrating 75 wt% Li<sub>1+x</sub>Al<sub>x</sub>Ge<sub>2-x</sub>(PO<sub>4</sub>)<sub>3</sub> into poly( $\epsilon$ -caprolactone) (PCL) [17]. In that report, the greatest ionic conductivity ( $1.7 \times 10^{-4} \text{ S cm}^{-1}$ ) was obtained for a LAGP concentration of 75 wt%, validating the “polymer-in-ceramic” concept. Lu et al. incorporated 50 wt% Li<sub>1+x</sub>Al<sub>x</sub>Ti<sub>2-x</sub>(PO<sub>4</sub>)<sub>3</sub> into a poly(vinylidene fluoride-co-hexafluoropropylene) (PVDF-HFP) polymer matrix to fabricate a flexible composite lithium-ion conducting membrane (FC-LICM) for use in HELABs with a cycling capacity of 500 mAh g<sup>-1</sup> for up to 80 h [25]. The utilization of SPE with a sodium super ionic conductor glass film type of filler in electrochemical devices has resulted in complaints about the interfacial stability between the SPE and the lithium metal [26–29].

Titanium dioxide (TiO<sub>2</sub>) has recently been suggested for use as an SPE because it is a classic inorganic filler that is easy to process, has a non-toxic nature, and has chemical compatibility [30,31]. The electrochemical behavior of TiO<sub>2</sub> has been extensively studied, including its electron transport, charge storage, and interfacial charge transfer [32]. The incorporation of TiO<sub>2</sub> provides a higher Li<sup>+</sup> ion transfer number owing to the enhanced interaction with the polymer and the promotion of Lewis acid–base interactions, which help establish ionic transport channels along the nanoparticles' surface rather than through the polymer segment [33,34]. Hwang et al. [35] reported that the SPE's electrolytic conductance increased with a reduction in the particles' size. Sasikumar et al. [36] chose a PVDF-HFP/polyvinyl acetate (PVAc) blend of polymer as the host, and a LiTFSi salt in the EC was added to increase the conductivity. They investigated various weight ratios (from 2.5 wt% to 10 wt%) of TiO<sub>2</sub> to PVDF-HFP/PVAc. The ionic conductivity progressively increased from  $1.1 \times 10^{-3} \text{ S cm}^{-1}$  to  $2.69 \times 10^{-3} \text{ S cm}^{-1}$  at a 7.5 wt% content and drastically dropped at 10 wt%, suggesting a percolation effect [37,38]. This result is ascribed to the dramatic decrease in the adsorption rate of the LE through the pore blockage with the further increase in the percentage of TiO<sub>2</sub> [39]. TiO<sub>2</sub>-incorporated SPEs using a polymer-rich configuration (with a TiO<sub>2</sub> content of 10% or less) are common in the literature [36,40].

Here, we present the fabrication of a solid electrolyte consisting of inorganic TiO<sub>2</sub> nanoparticles and a PVDF-HFP polymeric matrix. PVDF-HFP was selected as the host polymer owing to its chemical compatibility with lithium metal [41–44]. We investigated

a high load of  $\text{TiO}_2$  embedded into a polymer host to enhance ionic conductivity. We observed consistent improvements in the SPE's electrochemical impedance as the  $\text{TiO}_2$  load increased from 40 wt% to 60 wt% compared with the bare polymer. The assembled HELAB cycled for up to 70 h and beyond. The overpotential could be reduced by up to 33% during cycling compared with using bare polymer. This demonstrated that  $\text{TiO}_2$ -rich polymeric composites are effective solid electrolytes for application in HELABs. To the best of our knowledge, this is the first research using  $\text{TiO}_2$  as the inorganic nanoparticle in solid polymer electrolytes for application in a Li-air battery.

## 2. Experimental Section

### 2.1. Reagent

Lithium hydroxide monohydrate ( $\text{LiOH}\cdot\text{H}_2\text{O}$ ,  $\geq 99.0\%$ ), poly(vinylidene fluoride-co-hexafluoropropylene) (PVDF-HFP, M.W.  $\sim 455,000$ ), lithium bis(trifluoromethylsulfonyl) imide (LiTFSI, 99.95%), tetraethylene glycoldimethyl ether (TEGDME,  $\geq 99\%$ ), and commercial  $\text{TiO}_2$  powder (99.7%) were obtained from Sigma-Aldrich (St. Louis, MO, USA). Lithium chloride ( $\text{LiCl}$ , 99%) was purchased from Alfa Aesar (Ward Hill, MA, USA). N-methyl-2-pyrrolidone (NMP,  $\geq 99.0\%$ ) was purchased from Macron Fine Chemicals (Radnor, PA, USA).

### 2.2. Pretreatment and Fabrication of the FC-LICM Incorporating $\text{TiO}_2$

The commercial  $\text{TiO}_2$  powder was first wet ball-milled to optimize the distribution of particle size and the content of impurities. Ethanol was used as the medium. Figure S1 shows the effects of the powder's weight per batch and the ball-milling time on the derived size distribution of  $\text{TiO}_2$ . The distribution of the particles' size was measured using laser diffraction particle size analyzers (Mastersizer 2000, Malvern Panalytical, Worcestershire, UK) with a detection range of 0.02–2000  $\mu\text{m}$ . The dispersant's refractive index was adjusted to 1.36 to align with the ethanol medium. Figure S1 shows that the size distribution of  $\text{TiO}_2$  had the strongest red shift with 3 g of  $\text{TiO}_2$  during the process and when the ball-milling time was fixed at 48 h. Three grams of  $\text{TiO}_2$  were ball-milled at 400 rpm for 48 h. The ball-milled  $\text{TiO}_2$  was then passed through a 200-mesh sieve. The sieved sample was then collected with an ethanol wash. The derived  $\text{TiO}_2$  powder was thoroughly dispersed to form a stable white colloidal solution.

The FC-LICM comprising  $\text{TiO}_2$  and the PVDF-HFP matrix was derived using the simple blade-casting method. First, 3 g of PVDF-HFP were dissolved in 16 g of NMP under continuous stirring at 60  $^\circ\text{C}$ . The slurry solution was prepared using a simple solvent exchange route, as seen in Figure 1. The  $\text{TiO}_2$ /ethanol solution derived by ball-milling was added into the PVDF-HFP/NMP solution (with a weight ratio of  $\text{TiO}_2$ :PVDF-HFP = 1:1) with 30 min of sonication. This solution was then stirred at 120  $^\circ\text{C}$  for the complete removal of ethanol. The derived slurry was then cast onto a release film (H350A, Nan Ya Plastics Corp., Taipei, Taiwan) using a film casting knife with a clearance adjusted to 500  $\mu\text{m}$ . The cast film was dried in a vacuum at 60  $^\circ\text{C}$  for 3 days to form an FC-LICM.

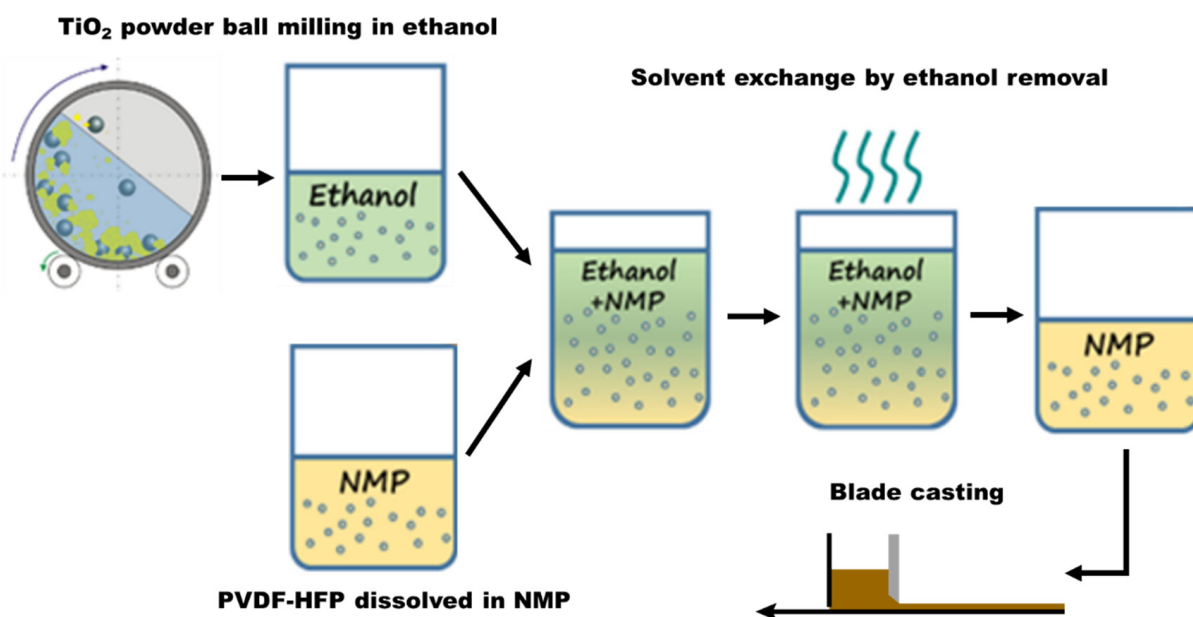


**Figure 1.** Schematic flow of preparing the flexible composite lithium-ion-conducting membrane (FC-LICM) consisting of poly(vinylidene fluoride-co-hexafluoropropylene) (PVDF-HFP) and titanium dioxide (TiO<sub>2</sub>) via the solvent exchange route.

### 2.3. Characterization of the Materials

The crystallinity was examined using X-ray diffraction (XRD) on a Bruker D2 Phaser (Bruker AXS GmbH, Karlsruhe, Germany) with Cu K $\alpha$  radiation ( $\lambda = 1.54 \text{ \AA}$ ) over the  $2\theta$  range of  $10\text{--}80^\circ$ . The microstructure of the as-fabricated FC-LICMs was studied using field emission scanning electron microscopy (FE-SEM, SU8000, Hitachi Ltd., Tokyo, Japan). Energy-dispersive X-ray spectroscopy (EDS) was carried out with an Xflash Detector 5030 (Bruker AXS GmbH, Karlsruhe, Germany) to determine the elemental distribution within the membrane. XPS (X-ray photoelectron spectroscopy) was performed with a K-Alpha X-ray Photoelectron Spectrometer at the R&D Center for Membrane Technology of Chung Yuan Christian University. The water permeation test was performed using a benchtop water quality meter (LAQUA F74, HORIBA, Kyoto, Japan) with a chloride ion electrode (6560S-10C). The as-fabricated FC-LICM was placed in between a glass module containing 50 mL of 2 M LiCl<sub>(aq)</sub> and 50 mL of water on the other side. The chloride ion electrode was immersed on the side of the water to measure the increase in the chloride concentration. The membrane's permeability was calculated using Equation (1) as follows:

$$\text{Permeability} = \frac{V}{A} \frac{L}{(C_0 - 0)} \frac{dC}{dt} \left( \frac{dC}{dt} > 0 \right) \quad (1)$$

where  $V$  is the volume of the solution,  $A$  is the cross-sectional area,  $L$  is the membrane's thickness, and  $C_0$  is the initial concentration of the feed. The percentage of swelling of the membrane was measured using the ratio of the diameter before and after immersion in the aprotic electrolyte (1.0 M LiTFSI in TEGDME).

### 2.4. Electrochemical Measurements and Assembly of the Hybrid Li–Air Battery

The charge transfer behavior of the dry FC-LICMs was measured using the AC impedance method by sandwiching the FC-LICMs between two stainless steel electrodes (with a diameter of 18 mm). The impedance was measured on an Autolab (PGSTAT302 N, Metrohm Autolab B.V., Utrecht, Netherlands) at an amplitude of 5 mV with a frequency

range of 0.1 Hz to 10 MHz at room temperature. The conductivity was calculated using the following Equation (2) [40]:

$$\sigma = \frac{L}{A \times R} \quad (2)$$

where  $L$  is the membrane's thickness,  $A$  is the membrane's area, and  $R$  is the resistance measured using the AC impedance test. In addition, the FC-LICMs were immersed in the aprotic electrolyte solution, and the impedance spectra were recorded on these wet FC-LICMs to investigate their charge transfer patterns.

The HELAB was constructed using CR-2032 coin cells (X2 Labwares Pte Ltd., Singapore) in a glove box (Unilab 3306-A, MBRAUN, Stratham, NH, USA). The anode side was composed of a Li metal foil (Biyuan Electronic Co., Ltd., Shenzhen, China) and a glass fiber (GF) porous separator (Whatman, Kent, UK, with a thickness of 420  $\mu\text{m}$ ) impregnated with 80  $\mu\text{L}$  of an aprotic electrolyte (1.0 M LiTFSI in TEGDME). The as-fabricated FC-LICM was inserted between the anode and the cathode. The cathode side consisted of a commercial Pt-coated carbon cloth with a load of 5  $\text{mg cm}^{-2}$  Pt (Yangtze Energy Technologies, Inc., New Taipei, Taiwan) and a polypropylene (PP) porous separator (Nippon Kodoshi Corp., Kochi, Japan, with a thickness of 100  $\mu\text{m}$ ) impregnated with 30  $\mu\text{L}$  of an aqueous catholyte (an aqueous solution of 1.0 M LiOH). The coin cells were cycled on a Model BAT-750B (AcuTech System Co., Ltd., New Taipei City, Taiwan) between 2.0 V and 4.5 V at a current density of 0.05  $\text{mA cm}^{-2}$  for 10 h per cycle when fed with ambient air (70–100% relative humidity) with a passive air-breathing mode.

### 3. Results and Discussion

#### 3.1. Characterization of $\text{TiO}_2$ Nanoparticle-Filled FC-LICMs

The effects of the ball-milling treatment were studied by measuring the size of the  $\text{TiO}_2$  using laser diffraction particle size analyzers. As seen in Figure S2, the size distribution of the  $\text{TiO}_2$  was reduced from 8  $\mu\text{m}$  to 90 nm on average. The broad peak around  $23^\circ$  in the XRD pattern was assigned to the background signal of the tape. The crystalline phase of  $\text{TiO}_2$  was ascribed to anatase crystals in the XRD analyses [45]. The size of the crystallite of the milled  $\text{TiO}_2$  was calculated to be 13.6 nm using Scherrer's formula. The larger size distribution, as shown by the light-scattering measurements (Figure S1), resulted from the aggregated  $\text{TiO}_2$  nanoparticles. Figure 2 shows the XPS spectrum of the as-prepared FC-LICM containing 50 wt%  $\text{TiO}_2$  nanoparticles. The 2p and O 1s peaks of Ti in addition to the C 1s and F 1s signals are present, indicating that the added  $\text{TiO}_2$  was successfully embedded into the polymer matrix. The Ti 2p<sub>1/2</sub> and 2p<sub>3/2</sub> peaks are shown in Figure S3.

The O 1s signal was observed as well, with the binding energy being the same as that of the commercial  $\text{TiO}_2$  powder. Note that the O 1s signal indicated a shoulder located toward higher binding energy, as seen in the commercial  $\text{TiO}_2$  powder. The secondary peak was assigned to hydroxyl ( $\text{OH}^-$ ) species according to the literature [46]. The peak fitting of C 1s is given in Figure 2. The spectrum has five main peaks at around 284, 285, 287, 290, and 292 eV, which were well defined [47–49]. As can be seen, the blending of  $\text{TiO}_2$  led to the spectra shifting to a higher binding energy, which was ascribed to the effect of  $\text{TiO}_2$  interacting with the polymer matrix. Table 1 shows a comparison of the ratio of the peak area between the  $-\text{CH}_2$  (predominantly influenced by vinylidene fluoride) and the  $-\text{CF}_2$  (predominantly influenced by hexafluoropropylene). The  $-\text{CH}_2$  became less prominent as the vinylidene fluoride segments were bonded to the embedded  $\text{TiO}_2$ .



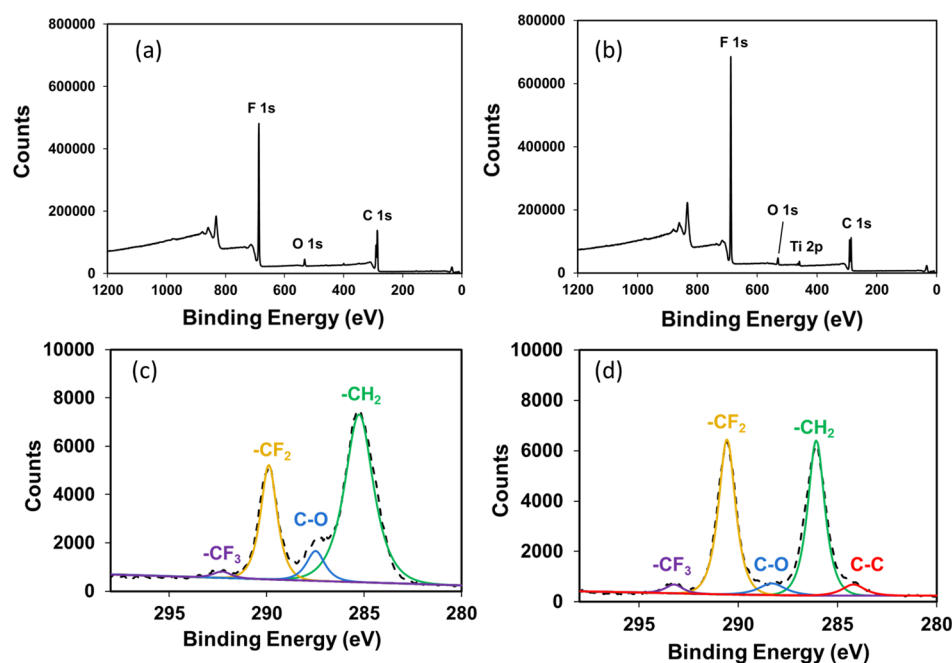


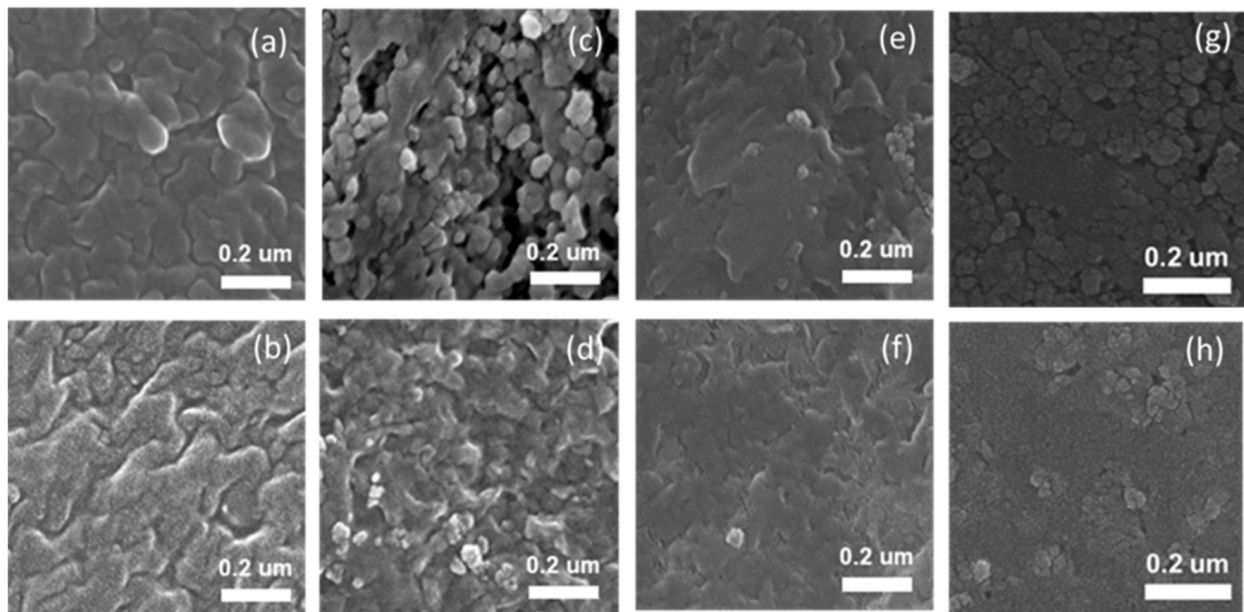
**Figure 2.** (a) XPS survey of the Al KR photoelectron spectra of (a) 0 wt% and (b) 50 wt% TiO<sub>2</sub> incorporated into the FC-LICM sample. High-resolution XPS C 1s peak spectra of (c) 0 wt% and (d) 50 wt%.

**Table 1.** Binding energy (B.E.) values and ratio of the peak area of -CH<sub>2</sub>- to -CF<sub>2</sub>- in the high-resolution C 1s spectra of FC-LICM.

Sample Name	B.E. (-CH <sub>2</sub> -)	B.E. (-CF <sub>2</sub> -)	Peak Area Ratio (-CH <sub>2</sub> - to -CF <sub>2</sub> -)
0 wt% of TiO <sub>2</sub> in FC-LICM	285.2 eV	289.8 eV	2.54
50 wt% of TiO <sub>2</sub> in FC-LICM	286 eV	290.5 eV	1

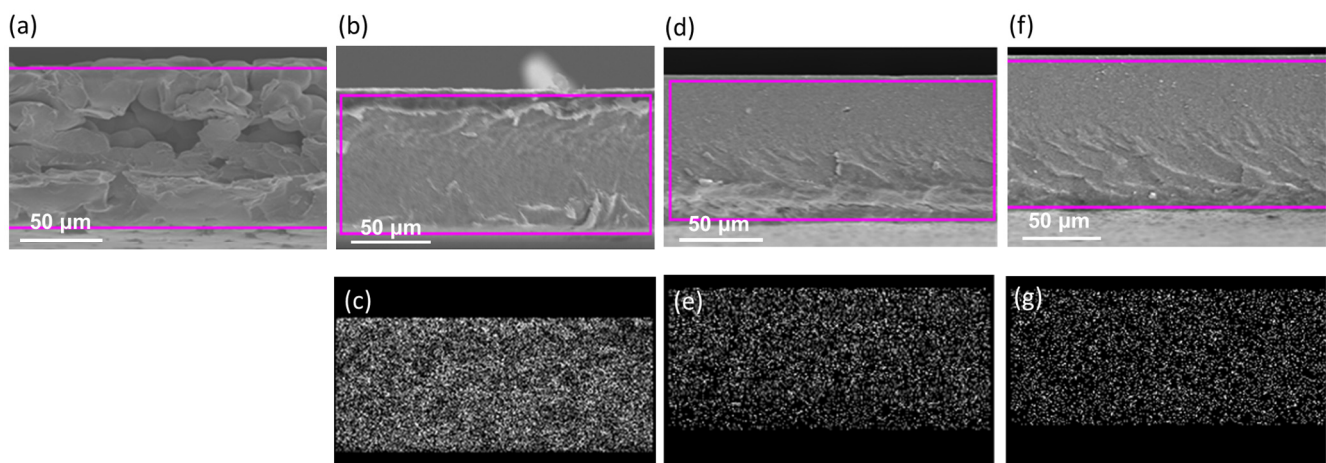
XRD and SEM analyses were carried out on the prepared FC-LICMs containing 40 wt%, 50 wt%, 60 wt% TiO<sub>2</sub> to identify the crystalline and morphological properties. Well-defined crystalline XRD patterns correlating to the standard database (TiO<sub>2</sub>, JCPDS PDF#021-1273) were observed for each proportion of TiO<sub>2</sub> (as shown in Figure S4). More importantly, the broader PVDF-HFP peak largely diminished in the FC-LICMs containing TiO<sub>2</sub>. This indicated that the addition of TiO<sub>2</sub> hindered the alignment of the polymer chain and led to a further decrease in the degree of crystallinity. According to Fahmi et al. [50], the appearance of an amorphous region or a reduction in the crystalline region can produce high ionic conductivity. The measured thermal stability and mechanical properties are shown in Figure S5. An early decomposition of the polymer around 350 °C was observed compared with that of the bare polymer (450 °C) in our thermal stability tests. This certified the reduced crystallization with the addition of TiO<sub>2</sub>. The FC-LICM with 50 wt% TiO<sub>2</sub> displayed a similar Young's modulus (295 MPa) to that of bare polymer (318 MPa).

Figure 3 shows the SEM images of the front (top images) and back (bottom images) of the tape-cast FC-LICM. The front side of the FC-LICM had a less dense surface with more pores in comparison with the back. A higher rate of bubble evaporation on the top resulted in the formation of pores during drying. This can best be seen in the FC-LICM with the incorporation of 40 wt% TiO<sub>2</sub>, for which more pores formed in comparison with the bare polymer. The voids help with the retention of the electrolyte, leading to higher conductivity [51].



**Figure 3.** SEM images (100 k) of the front and back side of the tape-cast FC-LICM with different proportions of  $\text{TiO}_2$ : (a,b) 0 wt%  $\text{TiO}_2$ , (c,d) 40 wt%  $\text{TiO}_2$ , (e,f) 50 wt%  $\text{TiO}_2$ , and (g,h) 60 wt%  $\text{TiO}_2$ .

Figure 4 shows the cross-sectional SEM images. EDS analyses were applied to display the distribution of Ti elements. It can clearly be seen that the Ti elements were well distributed across the cross-section, showing no partial deposition. Furthermore, a clearly rough cross-sectional morphology was observed in the pure polymer, which confirmed the reports in the literature [52]. Note that the cross-section micrograph changed entirely and became smooth with the addition of the nanoparticles, indicating a reduction in the crystallinity. Fahmi et al. reported that the reduction in crystallinity was caused by the distribution of random nanoparticles, which may introduce disorder in the electrolyte [50]. Thus, an increase in the conductivity of fabricated polymers with  $\text{TiO}_2$  nanoparticles was supported by the XRD results.



**Figure 4.** SEM cross-sectional images and EDS Ti mapping results of FC-LICMs containing (a) 0 wt%  $\text{TiO}_2$ , (b,c) 40 wt%  $\text{TiO}_2$ , (d,e) 50 wt%  $\text{TiO}_2$ , and (f,g) 60 wt%  $\text{TiO}_2$ .

### 3.2. Swelling Behavior and Permeating Properties of the As-Fabricated $\text{TiO}_2$ -Filled FC-LICMs

Permeation tests and tests of the swelling behavior were executed to identify the addition of  $\text{TiO}_2$  and the effects of different proportions of  $\text{TiO}_2$  on the prepared FC-LICMs. As shown in Table 2, the thicknesses were 94  $\mu\text{m}$ , 84  $\mu\text{m}$ , 86  $\mu\text{m}$ , and 90  $\mu\text{m}$  for FC-LICMs

containing 0 wt%, 40 wt%, 50 wt%, and 60 wt% TiO<sub>2</sub>, respectively. The results of the permeability test indicated that the FC-LICM without TiO<sub>2</sub> was the most waterproof among the candidates. The addition of TiO<sub>2</sub> decreased the membranes' compactness, allowing water to pass through in a short period of time. Among the TiO<sub>2</sub>-containing samples, the slowest permeability appeared at 50 wt% TiO<sub>2</sub>. When the TiO<sub>2</sub> content was increased to 60 wt%, more pores were produced as the largest permeability was observed at this concentration. According to these results, the TiO<sub>2</sub> content in the FC-LICMs is critical.

**Table 2.** Permeation and swelling tests for the FC-LICMs with 0 wt% TiO<sub>2</sub>, 40 wt% TiO<sub>2</sub>, 50 wt% TiO<sub>2</sub>, and 60 wt% TiO<sub>2</sub>.

TiO <sub>2</sub> Content in FC-LICM	Thickness (μm)	Permeability (cm <sup>2</sup> s <sup>-1</sup> )	Swelling Ratio (%) <sup>1</sup>	Aprotic Electrolyte Uptake (%) <sup>2</sup>
0 wt%	94	1.23 × 10 <sup>-9</sup>	8.5%	13.2%
40 wt%	84	5.12 × 10 <sup>-7</sup>	7.1%	11.8%
50 wt%	86	3.91 × 10 <sup>-7</sup>	4.7%	5.7%
60 wt%	90	1.13 × 10 <sup>-6</sup>	3.3%	2.7%

<sup>1</sup> Increase in thickness before and after immersion in the electrolyte. <sup>2</sup> Percentage of the membrane's weight before and after immersion in the electrolyte.

Moreover, the addition of TiO<sub>2</sub> mitigated the adsorption of the electrolyte and suppressed aprotic uptake after the FC-LICM was immersed into the aprotic electrolyte (1 M LiTFSI in TEGDME). Interestingly, these findings were not in line with the previous studies [36,51], in which composites exhibited enhanced electrolyte uptake upon the addition of filler. The swelling ratio and electrolyte uptake of the FC-LICM decreased under loading with TiO<sub>2</sub>.

### 3.3. Electrochemical Impedance Spectroscopy Analyses of FC-LICMs Filled with TiO<sub>2</sub>

EIS was performed to analyze the charge transfer ability of the as-prepared FC-LICMs in a dry state. A Nyquist plot for each FC-LICM is shown in Figure 5. An equivalent circuit model was developed to fit the data, and the results are shown in the red curves in Figure 5. The lower intercept of the semicircle, denoted R<sub>b</sub>, is contributed by the bulk resistance of the dry FC-LICM, as the contribution to the impedance of the external electrical wires was negligible. Significant decreases in R<sub>b</sub> were observed for the FC-LICM containing 40–60 wt% TiO<sub>2</sub>. The reduced R<sub>b</sub> can be ascribed to the semiconductive TiO<sub>2</sub> nanoparticles, which are more conductive compared with the bare polymer.

The diameter of the semicircle, denoted R<sub>ct</sub>, is associated with the charge transfer impedance of the sample [53]. As depicted in Figure 5, the radius of the arc of the impedance of the dry FC-LICMs was greatly reduced in the presence of a high load of TiO<sub>2</sub>. The R<sub>ct</sub> of the FC-LICM with 40 wt% TiO<sub>2</sub> was 70.3% less than that of the bare polymer (476 vs. 1609 Ω). The most effective improvement in R<sub>ct</sub> was obtained for the FC-LICM containing 50 wt% TiO<sub>2</sub>, with a 75.1% reduction in the R<sub>ct</sub> (from 1609 Ω to 420 Ω). However, the addition of excessive TiO<sub>2</sub> (60 wt%) did not reduce the R<sub>ct</sub> any further, possibly due to aggregation of the nanoparticles and a loss of the effective area for the electron charge transfer. Sasikumar et al. [36] reported that a high percentage of TiO<sub>2</sub> would reach a percolation threshold and cause aggregation of the particles, blocking the interfacial pathway of TiO<sub>2</sub>/electrolyte and suppressing the charge transfer. This finding demonstrates that the TiO<sub>2</sub>-loaded FC-LICMs possessed lower electron transport resistance and higher electron mobility. This result is in line with the literature [54], in which TiO<sub>2</sub> was reported to serve as an important “charge transfer bridge”. The composites with a high nanofiller loading provided sufficient interconnected pathways on the surfaces of the semiconductive TiO<sub>2</sub> particles for facilitating electron transport.



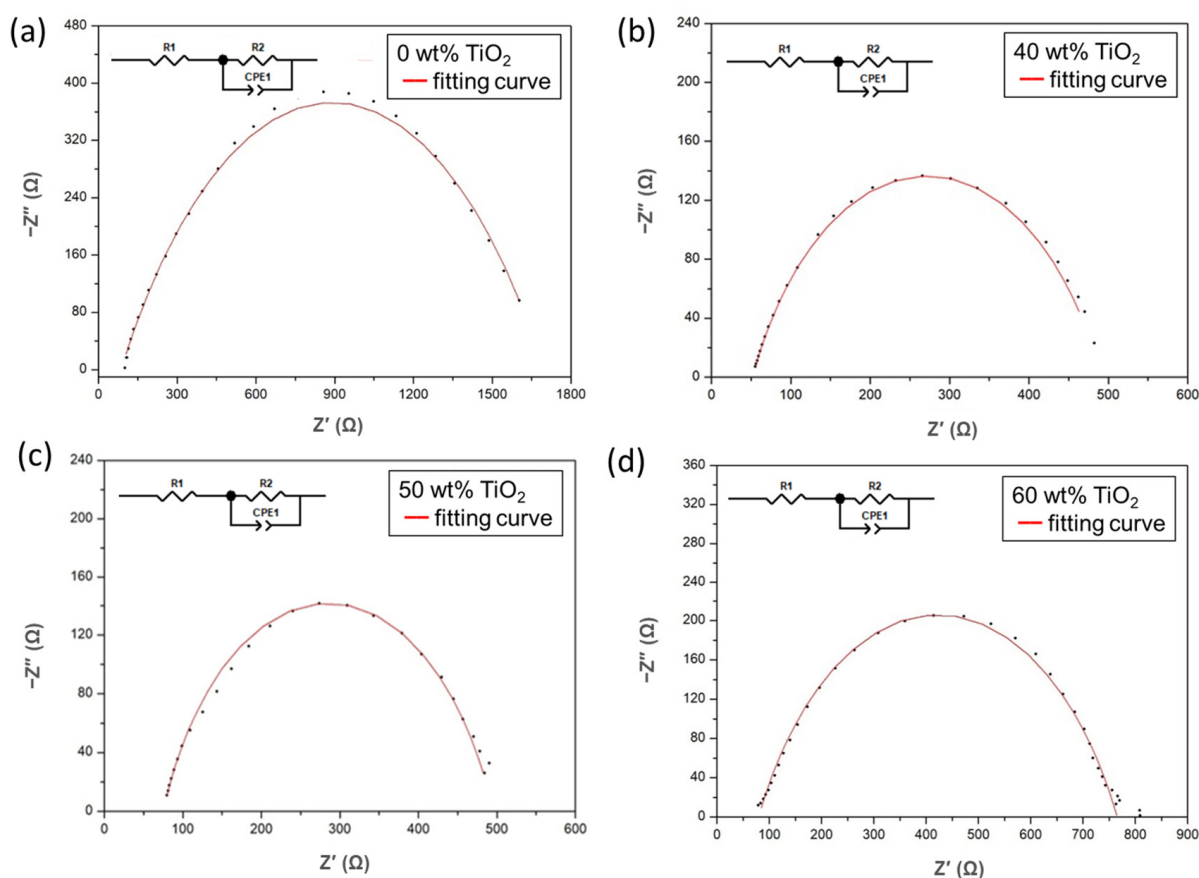


**Figure 5.** Nyquist plots of FC-LICMs with (a) 0 wt% TiO<sub>2</sub>, (b) 40 wt% TiO<sub>2</sub>, (c) 50 wt% TiO<sub>2</sub>, and (d) 60 wt% TiO<sub>2</sub> in a dry state.

To assemble the HELABs, the FC-LICM was used as a separator between the aprotic TEGDME electrolyte and the aqueous LiOH solution. The FC-LICM was immersed in an aprotic electrolyte and then characterized using impedance analysis. The spectra are shown in Figure 6, with the equivalent circuit models [55,56] shown in the insets. The first real impedance intercept below 100 Ω was denoted as R<sub>1</sub> and the second as R<sub>2</sub>. Both R<sub>1</sub> and R<sub>2</sub> values were several tens to several hundreds of ohms, much lower than the R<sub>b</sub> and R<sub>ct</sub> data in Table 3 (i.e., in the dry state) due to the presence of the lithium salt and the solvent. The FC-LICM containing 50 wt% TiO<sub>2</sub> demonstrated a reduction in R<sub>1</sub> from 63 to 43 Ω (a 32% decrease) compared with that without TiO<sub>2</sub>. The enhancement of R<sub>1</sub> in the TiO<sub>2</sub> composite can be ascribed to the increased amorphous phase region, as the TiO<sub>2</sub> nanofillers hindered the alignment and crystallization of the polymer chain. The electrolyte-immersed FC-LICM with 50% TiO<sub>2</sub> also indicated a decrease in R<sub>2</sub> from 141 to 76 Ω (45% less). The reduction in R<sub>2</sub> reflected the transport of additional lithium ions. The semiconductive TiO<sub>2</sub> nanoparticles served as a charge transfer bridge for transporting ions across the interface. The consistent results from Figures 5 and 6 implied that the TiO<sub>2</sub> nanoparticles in the FC-LICM facilitated the charge transfer for both electron transfer and ionic transport.

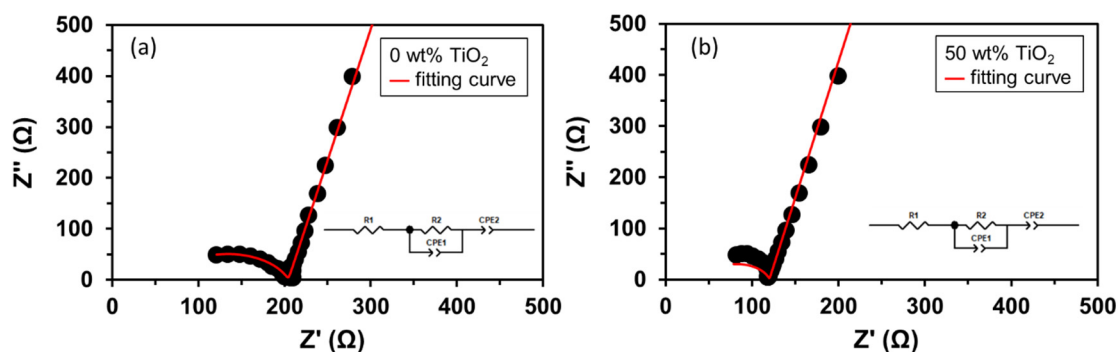


**Figure 6.** Nyquist plots of organic electrolyte-immersed FC-LICMs containing (a) 0 wt% TiO<sub>2</sub> and (b) 50 wt% TiO<sub>2</sub>.

**Table 3.** Impedance and conductivity results for the FC-LICMs with 0 wt% TiO<sub>2</sub>, 40 wt% TiO<sub>2</sub>, 50 wt% TiO<sub>2</sub>, and 60 wt% TiO<sub>2</sub> in a dry state.

TiO <sub>2</sub> Content in FC-LICM	R <sub>b</sub> (Ω)	R <sub>ct</sub> (Ω)	Conductivity (S cm <sup>-1</sup> )
0 wt%	85	1609	4.31 × 10 <sup>-5</sup>
40 wt%	48	476	6.86 × 10 <sup>-5</sup>
50 wt%	74	420	4.54 × 10 <sup>-5</sup>
60 wt%	79	685	4.43 × 10 <sup>-5</sup>

### 3.4. Cycling Performance of HELABs with Different Ratios of TiO<sub>2</sub>-Filled FC-LICMs

The battery performance of FC-LICMs incorporating TiO<sub>2</sub> was evaluated through an assembly of the HELAB and long-term discharge/charge testing. Figure 7 shows the cycling performance of HELABs with 0 wt%, 40 wt%, 50 wt%, and 60 wt% of TiO<sub>2</sub>-incorporated FC-LICMs. The HELAB using the TiO<sub>2</sub>-free FC-LICM showed the highest overpotential (2.33 V on average), indicating the most severe electrochemical resistance. This is in line with the inferior charge transfer shown in Table 3 and Figures 5 and 6. In contrast, the average overpotential was reduced to 1.85 V, 1.56 V, and 1.78 V for the HELABs with 40 wt%, 50 wt%, and 60 wt% TiO<sub>2</sub> filled FC-LICM, respectively. These values indicate reductions in the over-potential of 20.6%, 33%, and 23.6% compared with the bare FC-LICM. The presence of TiO<sub>2</sub> enhanced the interfacial charge transfer properties in the FC-LICM. The FC-LICM with 50 wt% TiO<sub>2</sub> demonstrated the highest charge transfer rate and the least overpotential in the HELAB cycling test.

Regarding the battery's lifetime, the FC-LICM containing 50 wt% TiO<sub>2</sub> displayed the longest cycle with a capacity of 500 mAh and 100% capacity retention for up to seven cycles (70 h), which was the same as for the FC-LICM without TiO<sub>2</sub> but with clearly higher round-trip efficiency. Earlier deterioration was found for the batteries with 40 wt% and 60 wt% TiO<sub>2</sub>. Deterioration occurred after six cycles (60 h) with a drastic decline in capacity. As discussed in Section 3.2, 50 wt% TiO<sub>2</sub> was more waterproof than 40 wt% TiO<sub>2</sub> and 60 wt% TiO<sub>2</sub>, meaning slower penetration of the LE. The 50 wt% TiO<sub>2</sub> proportion was more lasting because of the desired impenetrability of the FC-LICM. Overall, the failure of the battery should be ascribed to the crossover of the aqueous electrolyte and the eventual corrosion of the Li metal, which was irreversible. As seen in Figure 8, the Li metal was taken out of the dead HELABs and analyzed by XRD. The results showed that the Li metal was entirely corroded into LiOH compared with the active Li (Figure S6). The future challenge is to improve the membrane density of FC-LICM incorporating TiO<sub>2</sub> to achieve greater numbers of cycles.

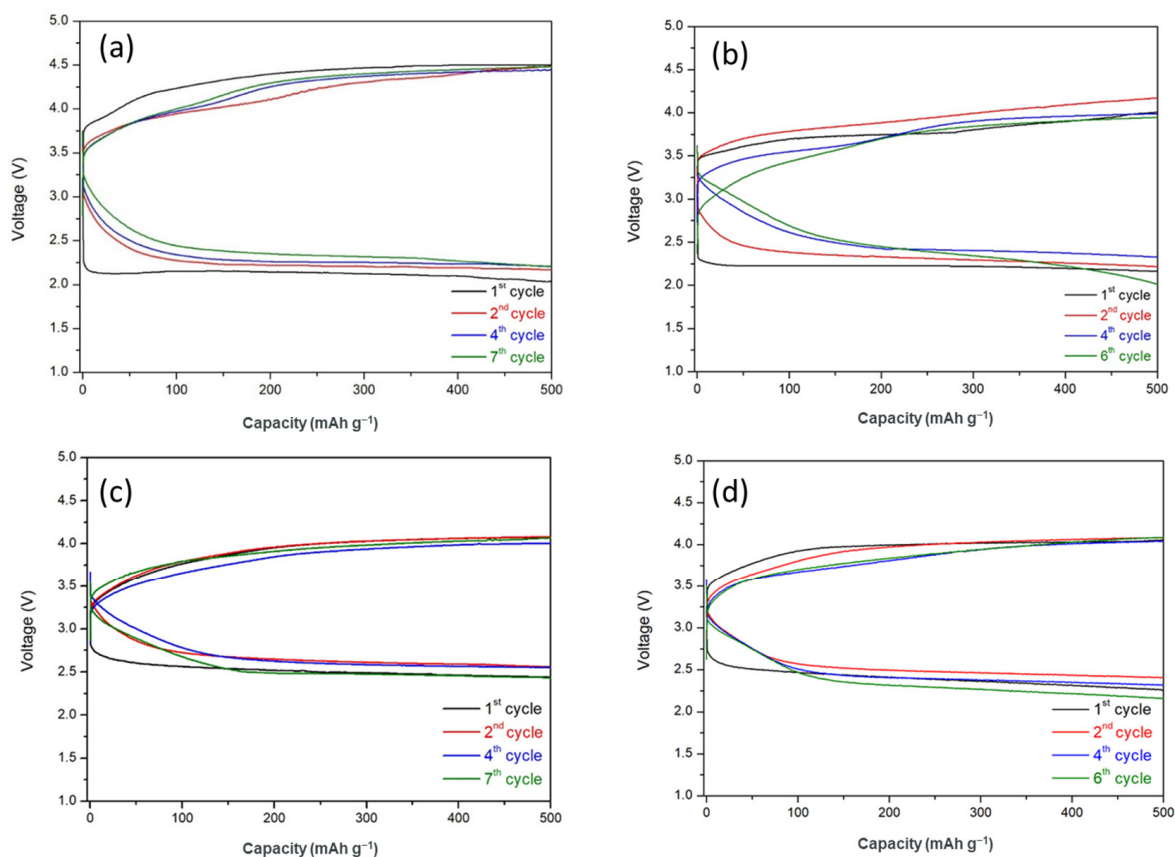


**Figure 7.** Long-term discharge/charge voltage profile of hybrid electrolyte Li-air batteries (HELABs) with FC-LICMs containing (a) 0 wt%, (b) 40 wt%, (c) 50 wt%, and (d) 60 wt%  $\text{TiO}_2$  under a constant current density of  $0.05 \text{ mA cm}^{-2}$  (with the charge and discharge capacities limited to  $500 \text{ mAh g}^{-1}$ ).

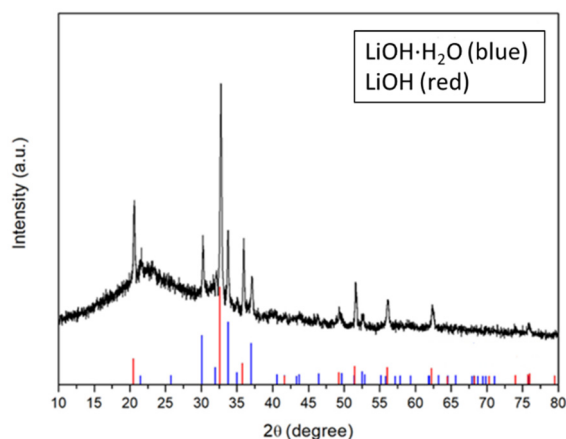


**Figure 8.** XRD pattern of the aged lithium anode after cycling of the HELAB.

Due to the appropriate addition of 50 wt%  $\text{TiO}_2$ , the assembled HELAB showed a 33% reduction in overpotential than that without  $\text{TiO}_2$  and provided the highest number of cycles among the FC-LICMs with various  $\text{TiO}_2$  loads. The higher cycling efficiency and reversibility without a clear capacity loss of the FC-LICM fabricated with 50 wt%  $\text{TiO}_2$  can be attributed to its higher charge transfer rate, the stable compatibility at the polymer- $\text{TiO}_2$  interface, and the desired water permeation barrier. Most encouragingly, our HELAB made from FC-LICM containing 50 wt%  $\text{TiO}_2$  demonstrated comparable numbers of cycles and lower overpotential (a reduction of 23% from 2.04 V to 1.56 V) than the HELAB with the NASICON-based FC-LICM [25] under the same operating conditions. We suggest that an

extra charge transfer path formed on the surface of the added TiO<sub>2</sub> nanoparticles, resulting in a significant increase in the capacity for charge transfer.

#### 4. Conclusions

This work demonstrated the preparation of a PVDF-HFP polymer with a high load semiconductive TiO<sub>2</sub> to form an elective electrolyte and separator in a hybrid electrolyte lithium–air battery (HELAB). A facile approach was used using a simple casting method and a solvent exchange process, followed by the ball-milling of the TiO<sub>2</sub> particles. A lower degree of polymer crystallinity was obtained by incorporating the TiO<sub>2</sub> nanoparticles. The presence of a high load of TiO<sub>2</sub> in the dry FC-LICM effectively promoted electron transport, as shown by the significant reduction in R<sub>ct</sub> (from 1609 Ω to 420 Ω) in comparison with the pristine PVDF-HFP. The FC-LICMs incorporating TiO<sub>2</sub> after infiltration of the aprotic electrolyte also exhibited a decrease in the charge transfer resistance of 45% compared with the bare polymer. These findings confirmed that the TiO<sub>2</sub> nanoparticles facilitated charge transfer for both electron transfer and ionic transport. The FC-LICM containing 50 wt% TiO<sub>2</sub> reduced the overpotential of the HELAB by 33% and was capable of cycling at 500 mA h beyond 70 h in a passive air-breathing mode under an atmosphere with high humidity.

**Supplementary Materials:** The supporting information can be downloaded at: <https://www.mdpi.com/article/10.3390/polym15102409/s1>. Figure S1. Ball milling conditions effects on prepared TiO<sub>2</sub> powder: (a) powder weight (b) ball milling time; Figure S2. TiO<sub>2</sub> powder refinement before-and-after 48 hours ball milling treatment: (a) powder size distribution (b) XRD result; Figure S3. High-resolution XPS spectrum of commercial TiO<sub>2</sub> powder:(a) Ti 2p peaks and (b) O 1s peak; and as-prepared 50 wt% TiO<sub>2</sub> FC-LICM of (c) Ti 2p and (d) O 1s; Figure S4. XRD result of 0 wt% TiO<sub>2</sub> and 50 wt% TiO<sub>2</sub> incorporated FC-LICM sample; Figure S5. (a) TGA result and (b) tensile result for 0 wt% and 50 wt% TiO<sub>2</sub> incorporated FC-LICM samples; Figure S6. XRD pattern of the pristine lithium anode.

**Author Contributions:** Conceptualization, H.-C.L.; Methodology, S.-H.P. and Y.-H.Y.; Validation, S.-H.P.; Formal analysis, S.-H.P. and S.J.L.; Investigation, Y.-H.Y.; Data curation, S.-H.P. and Y.-H.Y.; Writing—original draft, S.-H.P.; Writing—review & editing, H.-C.L. and S.J.L.; Visualization, S.-H.P.; Supervision, H.-C.L. and S.J.L.; Project administration, H.-C.L.; Funding acquisition, H.-C.L. and S.J.L. All authors have read and agreed to the published version of the manuscript.

**Funding:** This research was funded by National Science and Technology Council in Taiwan (MOST 109-2221-E-182-011-MY3 and MOST 111-2221-E-182-034-MY3).

**Informed Consent Statement:** Not applicable.

**Data Availability Statement:** Not applicable.

**Conflicts of Interest:** The authors declare no conflict of interest.

#### References

1. Heubner, C.; Nikolowski, K.; Reuber, S.; Schneider, M.; Wolter, M.; Michaelis, A. Recent insights into rate performance limitations of Li-ion batteries. *Batter. Supercaps* **2021**, *4*, 268. [[CrossRef](#)]
2. Kraysberg, A.; Ein-Eli, Y. Review on Li–air batteries—Opportunities, limitations and perspective. *J. Power Sources* **2011**, *196*, 886–893. [[CrossRef](#)]
3. Chen, Y.; Kang, Y.; Zhao, Y.; Wang, L.; Liu, J.; Li, Y.; Liang, Z.; He, X.; Li, X.; Tavajohi, N.; et al. A review of lithium-ion battery safety concerns: The issues, strategies, and testing standards. *J. Energy Chem.* **2021**, *59*, 83–99. [[CrossRef](#)]
4. Yoo, E.; Zhou, H. Li–air rechargeable battery based on metal-free graphene nanosheet catalysts. *ACS Nano* **2011**, *5*, 3020–3026. [[CrossRef](#)]
5. Christensen, A.; Albertus, P.; Sanchez-Carrera, R.S.; Lohmann, T.; Kozinsky, B.; Liedtke, R.; Ahmed, J.; Kojic, A. A critical review of Li/air batteries. *J. Electrochem. Soc.* **2012**, *159*, R1–R30. [[CrossRef](#)]
6. Aurbach, D.; McCloskey, B.D.; Nazar, L.F.; Bruce, P.G. Advances in understanding mechanisms underpinning lithium–air batteries. *Nat. Energy* **2016**, *1*, 16128. [[CrossRef](#)]
7. Wang, L.; Pan, J.; Zhang, Y.; Cheng, X.; Liu, L.; Peng, H. A Li–air battery with ultralong cycle life in ambient air. *Adv. Mater.* **2018**, *30*, 1704378. [[CrossRef](#)]

8. Zhao, Z.; Huang, J.; Peng, Z. Achilles Heel of lithium–air batteries: Lithium carbonate. *Angew. Chem. Int. Ed.* **2018**, *57*, 3874–3886. [[CrossRef](#)]
9. Zhang, W.; Nie, J.; Li, F.; Wang, Z.L.; Sun, C. A durable and safe solid-state lithium battery with a hybrid electrolyte membrane. *Nano Energy* **2018**, *45*, 413–419. [[CrossRef](#)]
10. He, H.; Niu, W.; Asl, N.M.; Salim, J.; Chen, R.R.; Kim, Y. Effects of aqueous electrolytes on the voltage behaviors of rechargeable Li-air batteries. *Electrochim. Acta* **2012**, *67*, 87–94. [[CrossRef](#)]
11. Sun, C.; Li, F.; Ma, C.; Wang, Y.; Ren, Y.; Yang, W.; Ma, Z.; Li, J.; Chen, Y.; Kim, Y.; et al. Graphene–Co<sub>3</sub>O<sub>4</sub> nanocomposite as an efficient bifunctional catalyst for lithium–air batteries. *J. Mater. Chem. A* **2014**, *2*, 7188. [[CrossRef](#)]
12. Manthiram, A.; Li, L. Hybrid and Aqueous Lithium–Air Batteries. *Adv. Energy Mater.* **2015**, *5*, 1401302. [[CrossRef](#)]
13. Peng, S.-H.; Chen, T.-H.; Li, C.-H.; Lu, H.-C.; Lue, S.J. Optimal cobalt oxide (Co<sub>3</sub>O<sub>4</sub>): Graphene (GR) ratio in Co<sub>3</sub>O<sub>4</sub>/GR as air cathode catalyst for air-breathing hybrid electrolyte lithium–air battery. *J. Power Sources* **2020**, *471*, 228373. [[CrossRef](#)]
14. Peng, S.-H.; Lu, H.-C.; Lue, S.J. Nanocrystal cobalt oxide (Co<sub>3</sub>O<sub>4</sub>) decorated graphene as efficient cathode catalyst for air-breathing hybrid electrolyte lithium–air battery. *Nanomaterials* **2020**, *10*, 1122. [[CrossRef](#)]
15. Hoang Huy, V.P.; So, S.; Hur, J. Inorganic fillers in composite gel polymer electrolytes for high-performance lithium and non-lithium polymer batteries. *Nanomaterials* **2021**, *11*, 614. [[CrossRef](#)]
16. Liu, W.; Liu, N.; Sun, J.; Hsu, P.C.; Li, Y.; Lee, H.W.; Cui, Y. Ionic conductivity enhancement of polymer electrolytes with ceramic nanowire fillers. *Nano Lett.* **2015**, *15*, 2740–2745. [[CrossRef](#)]
17. Zhang, B.; Liu, Y.; Liu, J.; Sun, L.; Cong, L.; Fu, F.; Mauger, A.; Julien, C.M.; Xie, H.; Pan, X. “Polymer-in-ceramic” based poly( $\epsilon$ -caprolactone)/ceramic composite electrolyte for all-solid-state batteries. *J. Energy Chem.* **2021**, *52*, 318–325. [[CrossRef](#)]
18. Hu, T.; Shen, X.; Peng, L.; Liu, Y.; Wang, X.; Ma, H.; Zhang, P.; Zhao, J. Preparation of single-ion conductor solid polymer electrolyte by multi-nozzle electrospinning process for lithium-ion batteries. *J. Phys. Chem. Solids* **2021**, *158*, 110229. [[CrossRef](#)]
19. Ge, Z.H.; Wei, K.; Lewis, H.; Martin, J.; Nolas, G.S. Bottom-up processing and low temperature transport properties of polycrystalline SnSe. *J. Solid State Chem.* **2015**, *225*, 354–358. [[CrossRef](#)]
20. Pignatelli, F.; Romero, M.; Castiglioni, J.; Faccio, R.; Momburá, A.W. Novel synergistic in situ synthesis of lithium-ion poly(ethylene citrate)-TiO<sub>2</sub> nanocomposites as promising fluorine-free solid polymer electrolytes for lithium batteries. *J. Phys. Chem. Solids* **2019**, *135*, 109082. [[CrossRef](#)]
21. Feng, Y.; Liu, X.; Liu, L.; Zhang, Z.; Teng, Y.; Yu, D.; Sui, J.; Wang, X. SiO<sub>2</sub>/C composite derived from rice husks with enhanced capacity as anodes for lithium-ion batteries. *Chem. Select.* **2018**, *3*, 10338–10344. [[CrossRef](#)]
22. Sun, C.; Liu, J.; Gong, Y.; Wilkinson, D.P.; Zhang, J. Recent advances in all-solid-state rechargeable lithium batteries. *Nano Energy* **2017**, *33*, 363–386. [[CrossRef](#)]
23. Long, L.; Wang, S.; Xiao, M.; Meng, Y. Polymer electrolytes for lithium polymer batteries. *J. Mater. Chem. A* **2016**, *4*, 10038–10069. [[CrossRef](#)]
24. Chen, L.; Li, Y.; Li, S.P.; Fan, L.Z.; Nan, C.W.; Goodenough, J.B. PEO/garnet composite electrolytes for solid-state lithium batteries: From “ceramic-in-polymer” to “polymer-in-ceramic”. *Nano Energy* **2018**, *46*, 176–184. [[CrossRef](#)]
25. Lu, S.-H.; Lu, H.-C. Pouch-type hybrid Li-air battery enabled by flexible composite lithium-ion conducting membrane. *J. Power Sources* **2021**, *489*, 229431. [[CrossRef](#)]
26. Hasegawa, S.; Imanishi, N.; Zhang, T.; Xie, J.; Hirano, A.; Takeda, Y.; Yamamoto, O. Study on lithium/air secondary batteries—Stability of NASICON-type lithium ion conducting glass–ceramics with water. *J. Power Sources* **2009**, *189*, 371–377. [[CrossRef](#)]
27. Zhang, T.; Imanishi, N.; Shimonishi, Y.; Hirano, A.; Takeda, Y.; Yamamoto, O.; Sammes, N. A novel high energy density rechargeable lithium/air battery. *Chem. Commun.* **2010**, *46*, 1661–1663. [[CrossRef](#)]
28. Imanishi, N.; Hasegawa, S.; Zhang, T.; Hirano, A.; Takeda, Y.; Yamamoto, O. Lithium anode for lithium-air secondary batteries. *J. Power Sources* **2008**, *185*, 1392–1397. [[CrossRef](#)]
29. Kumar, J.; Kumar, B. Development of membranes and a study of their interfaces for rechargeable lithium–air battery. *J. Power Sources* **2009**, *194*, 1113–1119. [[CrossRef](#)]
30. Zhang, L.; Lian, J.; Wu, L.; Duan, Z.; Jiang, J.; Zhao, L. Synthesis of a thin-layer MnO<sub>2</sub> nanosheet-coated Fe<sub>3</sub>O<sub>4</sub> nanocomposite as a magnetically separable photocatalyst. *Langmuir* **2014**, *30*, 7006–7013. [[CrossRef](#)]
31. Tseng, Y.; Ramdhani, F.; Hsiang, S.; Lee, T.; Teng, H.; Jan, J.S. Lithium battery enhanced by the combination of in-situ generated poly(ionic liquid) systems and TiO<sub>2</sub> nanoparticles. *J. Membr. Sci.* **2022**, *641*, 119891. [[CrossRef](#)]
32. Fabregat-Santiago, F.; Garcia-Belmonte, G.; Bisquert, J.; Zaban, A.; Salvador, P. Decoupling of transport, charge storage, and interfacial charge transfer in the nanocrystalline TiO<sub>2</sub>/electrolyte system by impedance methods. *J. Phys. Chem. B.* **2002**, *106*, 334–339. [[CrossRef](#)]
33. Liu, Y.; Lee, J.Y.; Hong, L. Morphology, crystallinity, and electrochemical properties of in situ formed poly(ethylene oxide)/TiO<sub>2</sub> nanocomposite polymer electrolytes. *J. Appl. Polym. Sci.* **2003**, *89*, 2815–2822. [[CrossRef](#)]
34. Jayanthi, S.; Kulasekarapandian, K.; Arulsankar, A.; Sankaranarayanan, K.; Sundaresan, B. Influence of nano-sized TiO<sub>2</sub> on the structural, electrical, and morphological properties of polymer-blend electrolytes PEO–PVC–LiClO<sub>4</sub>. *J. Compos. Mater.* **2014**, *49*, 1035–1045. [[CrossRef](#)]
35. Lin, C.W.; Hung, C.L.; Venkateswarlu, M.; Hwang, B.J. Influence of TiO<sub>2</sub> nano-particles on the transport properties of composite polymer electrolyte for lithium-ion batteries. *J. Power Sources* **2005**, *146*, 397–401. [[CrossRef](#)]



36. Sasikumar, M.; Hari Krishna, R.; Raja, M.; Therese, H.A.; Balakrishnan, N.T.M.; Raghavan, P.; Sivakumar, P. Titanium dioxide nano-ceramic filler in solid polymer electrolytes: Strategy towards suppressed dendrite formation and enhanced electrochemical performance for safe lithium ion batteries. *J. Alloy. Compd.* **2021**, *882*, 16070. [[CrossRef](#)]
37. Huo, H.; Zhao, N.; Sun, J.; Du, F.; Li, Y.; Guo, X. Composite electrolytes of polyethylene oxides/garnets interfacially wetted by ionic liquid for room-temperature solid-state lithium battery. *J. Power Sources* **2017**, *372*, 1–7. [[CrossRef](#)]
38. Kumar, B.; Scanlon, L.G. Polymer-ceramic composite electrolytes. *J. Power Sources* **1994**, *52*, 261–268. [[CrossRef](#)]
39. Yang, T.; Shu, C.; Zheng, R.; Li, M.; Hou, Z.; Hei, P. Dendrite-free solid-state Li–O<sub>2</sub> batteries enabled by organic–inorganic interaction reinforced gel polymer electrolyte. *ACS Sustain. Chem. Eng.* **2019**, *7*, 17362–17371. [[CrossRef](#)]
40. Song, D.Y.; Xu, C.; Chen, Y.F.; He, J.R.; Zhao, Y.; Li, P.J.; Lin, W.; Fu, F. Enhanced thermal and electrochemical properties of PVDF-HFP/PMMA polymer electrolyte by TiO<sub>2</sub> nanoparticles. *Solid State Ion.* **2015**, *282*, 31–36. [[CrossRef](#)]
41. Liang, X.; Han, D.; Wang, Y.; Lan, L.; Mao, J. Preparation and performance study of a PVDF–LATP ceramic composite polymer electrolyte membrane for solid-state batteries. *RSC Adv.* **2018**, *8*, 40498–40504. [[CrossRef](#)]
42. Kou, Z.; Miao, C.; Wang, Z.; Mei, P.; Zhang, Y.; Yan, X.; Jiang, Y.; Xiao, W. Enhanced ionic conductivity of novel composite polymer electrolytes with Li<sub>1.3</sub>Al<sub>0.3</sub>Ti<sub>1.7</sub>(PO<sub>4</sub>)<sub>3</sub> NASICON-type fast ion conductor powders. *Solid State Ionics* **2019**, *338*, 138–143. [[CrossRef](#)]
43. Hsia, T.; Lu, H.; Hsueh, Y.; Kumar, S.; Yen, C.; Yang, C.; Lue, S.J. Superdry poly (vinylidene fluoride-co-hexafluoropropylene) coating on a lithium anode as a protective layer and separator for a high-performance lithium-oxygen battery. *J. Colloid Interface Sci.* **2022**, *626*, 524–534. [[CrossRef](#)]
44. Wang, Y.; Huang, K.; Zhang, P.; Li, H.; Mi, H. PVDF-HFP based polymer electrolytes with high Li<sup>+</sup> transference number enhancing the cycling performance and rate capability of lithium metal batteries. *Appl. Surf. Sci.* **2022**, *574*, 151593. [[CrossRef](#)]
45. Wang, J.; Yu, J.; Zhu, X.; Kong, X.Z. Preparation of hollow TiO<sub>2</sub> nanoparticles through TiO<sub>2</sub> deposition on polystyrene latex particles and characterizations of their structure and photocatalytic activity. *Nanoscale Res. Lett.* **2012**, *7*, 646. [[CrossRef](#)]
46. Erdem, B.; Hunsicker, R.A.; Simmons, G.W.; Sudol, E.D.; Dimonie, V.L.; El-Aasser, M.S. XPS and FTIR surface characterization of TiO<sub>2</sub> particles used in polymer encapsulation. *Langmuir* **2001**, *17*, 2664–2669. [[CrossRef](#)]
47. Subianto, S.; Choudhury, N.; Dutta, N. Composite electrolyte membranes from partially fluorinated polymer and hyperbranched, sulfonated polysulfone. *Nanomaterials* **2013**, *4*, 1–18. [[CrossRef](#)]
48. Hinckley, A.C.; Wang, C.; Pfattner, R.; Kong, D.; Zhou, Y.; Ecker, B.; Bao, Z. Investigation of a solution-processable, nonspecific surface modifier for low cost, high work function electrodes. *ACS Appl. Mater. Interfaces.* **2016**, *8*, 19658–19664. [[CrossRef](#)]
49. Kaspar, P.; Sobola, D.; Částková, K.; Knápek, A.; Burda, D.; Orudzhev, F.; Hadaš, Z. Characterization of polyvinylidene fluoride (Pvdf) electrospun fibers doped by carbon flakes. *Polymers* **2020**, *12*, 2766. [[CrossRef](#)]
50. Fahmi, E.M.; Ahmad, A.; Rahman, M.Y.A.; Hamzah, H. Effect of NiO nanofiller concentration on the properties of PEO-NiO-LiClO<sub>4</sub> composite polymer electrolyte. *J. Solid State Electrochem.* **2012**, *16*, 2487–2491. [[CrossRef](#)]
51. Sasikumar, M.; Jagadeesan, A.; Raja, M.; Hari Krishna, R.; Sivakumar, P. The effects of PVAc on surface morphological and electrochemical performance of P(VdF-HFP)-based blend solid polymer electrolytes for lithium ion-battery applications. *Ionics* **2019**, *25*, 2171–2181. [[CrossRef](#)]
52. Kim, K.M.; Ko, J.M.; Park, N.G.; Ryu, K.S.; Chang, S.H. Characterization of poly (vinylidene fluoride-co-hexafluoropropylene)-based polymer electrolyte filled with rutile TiO<sub>2</sub> nanoparticles. *Solid State Ion.* **2003**, *161*, 121–131. [[CrossRef](#)]
53. Kim, H.S.; Mora-Sero, I.; Gonzalez-Pedro, V.; Fabregat-Santiago, F.; Juarez-Perez, E.; Park, N.G.; Bisquert, J. Mechanism of Carrier Accumulation in Perovskite Thin-absorber Solar Cells. *Nat. Commun.* **2013**, *4*, 2242. [[CrossRef](#)] [[PubMed](#)]
54. Jiao, Z.; Shang, M.; Liu, J.; Lu, G.; Wang, X.; Bi, Y. The charge transfer mechanism of Bi modified TiO<sub>2</sub> nanotube arrays: TiO<sub>2</sub> serving as a “charge-transfer-bridge”. *Nano Energy* **2017**, *31*, 96–104. [[CrossRef](#)]
55. Barsoukov, E.; Macdonald, J.R. *Impedance Spectroscopy: Theory, Experiment, and Applications*; Wiley: Hoboken, NJ, USA, 2005.
56. Sassmann, P.B.; Weichold, O. Preparation and characterisation of ion-conductive unsaturated polyester resins for the on-site production of resistivity sensors. *Ionics* **2019**, *25*, 3971–3978. [[CrossRef](#)]

**Disclaimer/Publisher’s Note:** The statements, opinions and data contained in all publications are solely those of the individual author(s) and contributor(s) and not of MDPI and/or the editor(s). MDPI and/or the editor(s) disclaim responsibility for any injury to people or property resulting from any ideas, methods, instructions or products referred to in the content.